Journal of Nanobiotechnology

RESEARCH Open Access

Regulating electron transportation by tungsten oxide nanocapacitors for enhanced radiation therapy

Hongbo Gao[1†], Li Sun[1†], Dalong Ni[2], Libo Zhang[3], Han Wang[2], Wenbo Bu[4], Jinjin Li[5], Qianwen Shen[1], Ya Wang[4], Yanyan Liu[4*] and Xiangpeng Zheng[1*]

Abstract

In the process of radiation therapy (RT), the cytotoxic effects of excited electrons generated from water radiolysis tend to be underestimated due to multiple biochemical factors, particularly the recombination between electrons and hydroxyl radicals (·OH). To take better advantage of radiolytic electrons, we constructed WO_3 nanocapacitors that reversibly charge and discharge electrons to regulate electron transportation and utilization. During radiolysis, WO_3 nanocapacitors could contain the generated electrons that block electron-·OH recombination and contribute to the yield of ·OH at a high level. These contained electrons could be discharged from WO_3 nanocapacitors after radiolysis, resulting in the consumption of cytosolic NAD^+ and impairment of NAD^+-dependent DNA repair. Overall, this strategy of nanocapacitor-based radiosensitization improves the radiotherapeutic effects by increasing the utilization of radiolytic electrons and ·OH, warranting further validation in multiple tumour models and preclinical experiments.

Keywords Tungsten oxide, Cancer, Radiotherapy, Nanotechnology, Pseudocapacitor

Introduction

Radiation therapy (RT) is one of the most effective cytotoxic therapies for the treatment of malignant tumours, and approximately 60% of patients receive radiotherapy in different treatment stages despite advances in many other treatment modalities [1–3]. Basically, the interaction between X-rays and genetic materials (mainly DNA molecules) contributes to cancer cell death. Radiation photons can generate direct damage to DNA or react with adjacent water molecules to produce highly reactive hydroxyl radicals (·OH) followed by DNA damage (the indirect mechanism) [4–8]. It has been recognized that the majority of X-ray damage to DNA in mammalian cells is caused by ·OH. In addition to ·OH, free electrons are also produced during the radiolysis of H_2O. Despite potential contributions to DNA damage, these free electrons have negative impacts on the collective radiation

†Hongbo Gao and Li Sun these authors contributed equally to this work.

*Correspondence:
Yanyan Liu
liuyyan@fudan.edu.cn
Xiangpeng Zheng
zhengxp@fudan.edu.cn
[1]Department of Radiation Oncology, Shanghai Huadong Hospital, Fudan University, Shanghai 200040, China
[2]Department of Orthopaedics, Shanghai Key Laboratory for Prevention and Treatment of Bone and Joint Diseases, Shanghai Institute of Traumatology and Orthopaedics, Ruijin Hospital, Shanghai Jiao Tong University School of Medicine, Shanghai 200025, China
[3]Department of Radiology, The First Affiliated Hospital of Soochow University, Suzhou 215006, China
[4]Department of Material Science and State Key Laboratory of Molecular Engineering of Polymers, Fudan University, Shanghai 200433, China
[5]Shanghai Key Laboratory of Green Chemistry and Chemical Processes, School of Chemistry and Molecular Engineering, East China Normal University, Shanghai 200062, China

effects due to recombination with ·OH and resultant neutralization of ·OH [9–12]. Hence, it is theorized to interfere with or block the recombination process of electrons and ·OH to take better advantage of both electrons and ·OH to improve the clinical outcome of radiotherapy.

The DNA damage response (DDR) is the cellular self-defence response to DNA damage with attempts to recover the integrity of DNA molecules, which apparently compromises radiotherapeutic efficacy [13–15]. As the most common type of DNA damage, DNA single-strand breaks (SSBs) tend to be readily repaired by the PARP-1-mediated signalling pathway, and NAD^+ exerts a critical role in the process of activating this pathway [16–18]. Reducing NAD^+ to NADH can effectively suppress the repair of DNA SSBs, and unrepaired DNA SSBs can transform into DNA double-strand breaks (DSBs) at replication forks, which may be irreparable or difficult to repair and ultimately fatal to cells [19]. Thus, it would be ideal to instruct radiolytic electrons to react with NAD^+, which not only separates electrons and ·OH to increase the utilization efficiency of ·OH but also simultaneously reduces the intracellular NAD^+ content to suppress DNA SSB repair. However, considering the supershort lifetime of radiolytic electrons (typically at the microsecond level), the reaction window between NAD^+ and electrons is extremely narrow under natural conditions [19, 20]. How to transfer radiolytic electrons to NAD^+ remains a significant issue to be solved.

In light of their unique performance in electron storage and release, supercapacitors have been widely studied in renewable energy fields for decades [21, 22]. Among various supercapacitors, WO_3, RuO_3 and MnO_2 have received much attention due to their high capacitance and energy density [23–27]. During the pseudocapacitance reaction, metal ions reversibly absorb and release electrons for time-space resolved regulation of electrons [28, 29]. This process suggests that pseudocapacitors may have potential medical use by regulating electron transportation by reversibly storing and releasing X-ray-induced electrons to extend their lifetime to overcome the above mentioned issues related to radiolytic electrons.

Herein, we report the experimental results of WO_3 nanocapacitors as electron regulators for radiosensitization. As demonstrated in Fig. 1, during the process of radiolysis, WO_3 nanocapacitors accepts radiolytic electrons (charging), which reduces the probability of recombination between ·OH and electrons to maintain cytosolic/nucleic ·OH at a high level. Subsequently, these electrons are discharged from nanocapacitors to react with endogenous NAD^+, potentially resulting in NAD^+-dependent reduced PARP-1-mediated DNA SSB repair. Collectively, the employment of WO_3 nanocapacitors enhances radiation-induced DNA damage and radiotherapeutic effects.

Methods

Reagents

$Na_2WO_4{\cdot}2H_2O$, citric acid and glucose were purchased from Adamas-beta. Hydrochloric acid (37%) was obtained from Sinopharm. $LuCl_3{\cdot}6H_2O$ was purchased from Sigma–Aldrich. Rhodamine B (RhB) was purchased from TCI. The aminophenyl fluorescein (APF) probe was purchased from AAT Bioquest. Phosphate buffered solution (PBS), Dulbecco's modified Eagle medium (DMEM) and foetal bovine serum (FBS) were obtained from Gibco. Cell counting kit-8 (CCK-8), histone H_2AX rabbit polyclonal antibody, DAPI staining kit, annexin V-FITC apoptosis detection kit, haematoxylin and eosin (H&E) staining kit, NADH/NAD^+ assay kit with WST-8 and TUNEL apoptosis assay kit were purchased from Beyotime.

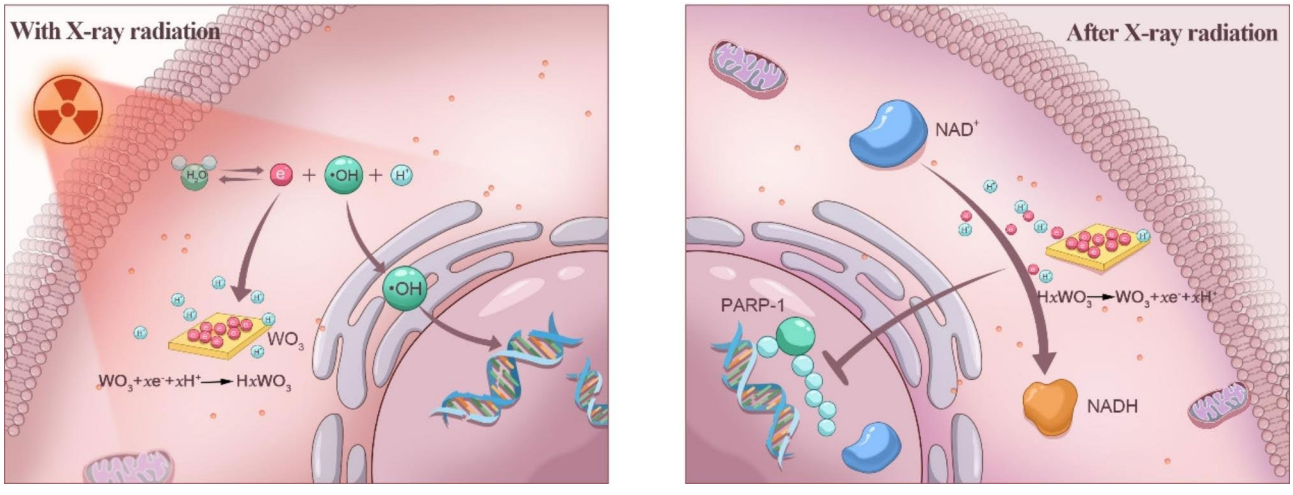

Fig. 1 Illustration of the mechanism that regulating electron transportation by WO_3 nanocapacitors for enhanced radiation therapy

Cells and animals

Lewis cancer cells (mouse lung cancer cells), RAW264.7 and H9C2 cells were purchased from Shanghai Institute of Biochemistry and Cell Biology, Chinese Academy of Sciences. Kunming mice and Balb/c nude mice were purchased from Shanghai SLAC Laboratory Animal Co. Ltd. These mice were raised in the Laboratory Animal Center of Fudan University. All in vivo experiments were approved by the Animal Care Committee of Laboratory Animals of Fudan University.

Experimental apparatus

A transmission electron microscope (TEM) graph was obtained from FEI Tecnai G2 F30. X-ray diffraction (XRD) was measured by Rigaku D/MAX-2250 V. The UV−Vis absorption spectrum was measured by Shimadzu UV-3600 Plus. Inductively coupled plasma−optical emission spectrometry (ICP−OES) was measured by Agilent Technologies 5100. The electrochemical workstation was CHI660E. Confocal laser scanning microscopy was carried out on a Nikon $A1^{+}R$-980. The fluorescence microplate system was TECAN SPARK. The fluorescence spectrometer was an Edinburgh Instruments FLS 980. Dynamic light scattering (DLS) was measured by a Malvern ZEN1600. Deionized (DI) water was obtained from ELGA CENTRA. The flow cytometer was a Beckman CytoFlex S. Radiation therapy was carried out by a Varian Clinac 21EX (Trilogy), which was applied in the clinic at Huadong Hospital affiliated with Fudan University. X-rays (6 MeV) were used for all experiments, and the dose rate was 5 Gy/min.

Synthesis of WO_3 nanocapacitors

60 mL deionized water, 3 mmol citric acid, 2 mmol $Na_2WO_4{\cdot}2H_2O$ and 10 mmol glucose were mixed and stirred until the solution was clear. Then, this solution was poured into a 100 mL hydrothermal synthesis reactor and stirred. After the slow and dropwise addition of 3.6 mL hydrochloric acid, this mixture was stirred for another 30 min. Then, this reactor was placed in a heating box at 120 ℃ for 20 h to obtain WO_{3-x}. After the reaction, the supernatant in the reactor was discarded. The obtained WO_{3-x} at the bottom was rinsed with deionized water and collected via high-speed centrifugation three times. To eliminate oxygen vacancies, WO_{3-x} was calcined at 500 ℃ for 10 h. Finally, the obtained pale yellow powder was a WO_3 nanocapacitor.

Electrochemical measurements

The electrolyte was 0.5 mol/L aqueous H_2SO_4. The reference electrode was a Ag/AgCl electrode. The counter electrode was a Pt electrode. The current collector was carbon cloth, and the area was 1 cm^2. Each carbon cloth contained 4 mg WO_3. For cyclic voltammetry (CV), the scan rates were 5, 10, 20, 40, 60, 80 and 100 mV/s. For galvanostatic charge−discharge (GCD) measurements, the current densities were 0.5, 2.0, 5.0 and 10.0 A/g, respectively. Cycle performance was measured by GCD at 5.0 A/g. The applied potential window ranged from −0.65 to 0.05 V. The frequency range of the electrochemical impedance spectra (EIS) was 0.01 to 10^5 Hz with an amplitude of 10 mV. The specific capacitance of WO_3 was calculated by GCD.

Detection of •OH in solutions and in vitro

The yield of •OH was detected by the degradation of RhB. A single RhB solution (10 mg/L), WO_3 (total mass 231.85 mg/L, W 1 mmol/L) solution containing RhB (10 mg/L), $Na_2WO_4{\cdot}2H_2O$ (total mass 329.86 mg/L, W 1 mmol/L) solution containing RhB (10 mg/L), and $LuCl_3{\cdot}6H_2O$ (total mass 389.42 mg/L, Lu 1 mmol/L) solution containing RhB (10 mg/L) were prepared. Then, these solutions were transferred into 96-well plates (100 μL/well) and irradiated with 0 Gy, 5 Gy, 10 Gy, 15 Gy, 20 and 25 Gy X-rays (6 MeV, 5 Gy/min). The absorbance of RhB at 564 nm was measured via a microplate spectrophotometer. The decrease in the absorbance of RhB represented the yield of •OH. For the in vitro experiments, Lewis cells (1×10^4 cells/well) were seeded in confocal dishes and incubated with RPMI-1640 medium, $Na_2WO_3{\cdot}2H_2O$ (28.5 μg/mL) and WO_3 nanocapacitors (20 μg/mL) for 12 h. Then, the culture medium was replaced with culture medium containing HPF (5 μmol/L) and incubated for 0.5 h. Afterwards, these dishes were irradiated with 4 Gy X-rays. Finally, the fluorescence of the HPF probe was observed by confocal fluorescence microscopy.

Computer simulation

We employed first principles to perform density functional theory (DFT) calculations within the generalized gradient approximation (GGA) using the Perdew-Burke-Ernzerhof (PBE) formulation. We have chosen the projected augmented wave (PAW) potentials to describe the ionic cores and take valence electrons into account using a plane wave basis set with a kinetic energy cut-off of 500 eV. Partial occupancies of the Kohn−Sham orbitals were allowed using the Gaussian smearing method and a width of 0.05 eV. The electronic energy was considered self-consistent when the energy change was smaller than 10^{-6} eV. A geometry optimization was considered convergent when the energy change was smaller than 0.02 eV/Å. In the process of simulating the crystal surface calculation, to avoid repetition for surface interaction, the vacuum spacing in the discontinuous direction was 15 Å for the (110) slab. In all the calculations, we use 6×6×4 for the Monkhorst-Pack k-point for the periodic interface

model. We created W^{5+} by building an O vacancy model with a low concentration in the WO_3 structure.

Stability of WO_3 nanocapacitors

WO_3 nanocapacitors were dispersed in RPMI-1640 medium (concentration: 200 μg/mL). After 1 day, 5 days and 10 days, we characterized the hydrodynamic radius of each sample. For detecting the release of W atoms, we measured the concentration of W of supernatant by ICP-OES, which was collected via high-speed centrifugation.

Cell viability

Lewis cells (1×10^4 cells/well) were seeded in 96-well plates and cultured at 37 °C for 24 h. Then, the culture medium was replaced with fresh RPMI-1640 medium containing WO_3 nanocapacitors at various concentrations (0, 6.25, 12.5, 25, 50, 100, 200, 400 μg/mL) and cultured for another 24 h. Then, the medium was discarded, and the cells were washed with PBS. Then, 100 μL of medium containing 10 μL of CCK-8 solution was added and coincubated for 2 h. Finally, the absorbance was measured by a microplate reader at 450 nm. The in vitro cytotoxicity of WO_3 nanocapacitors to normal cells (RAW264.7 and H9C2 cells) was also assessed using a similar protocol.

Detection of NAD^+ in vitro

The NAD^+ content in vitro was measured using WST-8 assays. Lewis cells were seeded in six-well plates and incubated with RPMI-1640 medium, $Na_2WO_3{\cdot}2H_2O$ (28.5 μg/mL) and WO_3 nanocapacitors (20 μg/mL) for 12 h. Then, the cells were treated with 4 Gy X-rays. After 0.5 h, the NAD^+/NADH ratio was measured with an NAD^+/NADH assay kit. The absorbance of solutions at 450 nm was measured by a microplate spectrophotometer, which presented the content of NAD+/NADH.

Detection of PAR in vitro

Lewis cells (1×10^4 cells/well) were seeded in confocal dishes and cultured for 24 h. Then, the cells were incubated with RPMI-1640 medium, $Na_2WO_3{\cdot}2H_2O$ (28.5 μg/mL) and WO_3 nanocapacitors (20 μg/mL) for another 24 h. Next, these cells were irradiated with 4 Gy X-rays. After 0.5 h, the cells were fixed with 4% paraformaldehyde for 10 min and washed with PBS three times. Then, 0.2% Triton X-100 was added to penetrate cells for 10 min. Afterwards, the cells were blocked with 1% BSA for 1 h. After incubation with PAR antibody for 12 h at 4 °C, the cells were treated with anti-rabbit IgG (H+L) and F(ab')2 Fragment (Alexa Fluor®594 Conjugate) for 1 h and then stained with DAPI for 15 min. Finally, the fluorescence of PAR was observed using a confocal fluorescence microscope.

Western blot analysis

Lewis cells (1×10^5 cells/well) were seeded in 6-well plates for 24 h. Then, the cells were incubated with RPMI-1640 medium, $Na_2WO_3{\cdot}2H_2O$ (28.5 μg/mL) and WO_3 nanocapacitors (20 μg/mL) for another 24 h. Next, these cells were irradiated with 4 Gy X-rays and washed with PBS three times. The cells were all lysed with RIPA buffer (Absin) supplemented with PMSF buffer (Absin). Protein concentration was tested by using a BCA protein assay kit (Beyotime Biotechnology). Equal amounts of proteins were separated by sodium dodecyl sulfate–polyacrylamide gel electrophoresis (SDS–PAGE) and then transferred to nitrocellulose (NC) membranes (Pall Corp.) and incubated overnight with primary antibodies at 4 °C followed by blocking with bovine serum albumin (BSA) (5%, v/v). The primary antibodies included Anti-PARP1 (rabbit, Abcam, ab32138, 1:1000), Poly/Mono-ADP Ribose (rabbit, CST, 83,732 S, 1:1000) and Gapdh (rabbit, Abways, AB0037, 1:5000). The membranes were probed with relevant secondary antibodies and scanned by 492 Odyssey instruments (LI-COR).

Detection of DNA DSBs in vitro

Lewis cells (1×10^4 cells/well) were seeded in confocal dishes and cultured for 24 h. Then, the cells were incubated with RPMI-1640 medium, $Na_2WO_3{\cdot}2H_2O$ (28.5 μg/mL) and WO_3 nanocapacitors (20 μg/mL) for another 24 h. Next, these cells were irradiated with 4 Gy X-rays. Subsequently, the cells were fixed with 4% paraformaldehyde for 10 min and washed with PBS three times. Then, 0.2% Triton X-100 was added to penetrate cells for 10 min. Afterwards, the cells were blocked with 1% BSA for 1 h. After incubation with γ-H_2AX antibody for 12 h at 4 °C, the cells were treated with anti-rabbit IgG (H+L), F(ab')2 fragment (Alexa Fluor®488 Conjugate) for 1 h and then stained with DAPI for 15 min. Finally, the fluorescence of γ-H_2AX was observed using a confocal fluorescence microscope.

Flow cytometry assay

Lewis cells (1×10^5 cells/well) were seeded in 6-well plates for 24 h. Next, these cells were incubated with RPMI-1640 medium, $Na_2WO_3{\cdot}2H_2O$ (28.5 μg/mL) and WO_3 nanocapacitors (20 μg/mL) for another 24 h. Then, the cells were irradiated with 4 Gy X-rays and washed with PBS three times. After incubation with RPMI-1640 for 24 h, the cells were stained with Annexin V-FITC and PI. Finally, cell apoptosis was measured by flow cytometry.

Cell clone formation assay

Lewis cells were seeded in 6-well plates (200, 200, 400, and 800 cells per well) for 24 h. Next, the cells were incubated with RPMI-1640 medium, $Na_2WO_3{\cdot}2H_2O$ (28.5 μg/mL) and WO_3 nanocapacitors (20 μg/mL) for another

24 h and subsequently exposed to 0 Gy, 2 Gy, 4 Gy, and 6 Gy X-rays. After culturing for 10 days, the cells were fixed with methyl alcohol and stained with haematoxylin and eosin. The number of colonies was counted by ImageJ.

In vivo biocompatibility assay

To detect the biocompatibility of WO_3 nanocapacitors, blood parameter analysis and standard H&E staining were conducted using Kunming mice (7 weeks, female). After injection with WO_3 nanocapacitors (50 mg/kg) via the tail vein, the main tissues (heart, liver, spleen, lung and kidney) of Kunming mice were obtained for H&E staining, and blood was harvested for routine blood tests and biochemical examination at 2 days and 30 days postinjection. The control group received intravenous PBS only and was sacrificed at 2 days and 30 days for the same assays.

In vivo blood terminal half-life and biodistribution of WO_3 nanocapacitors

To assay the blood terminal half-life of WO_3 nanocapacitors in vivo, three Kunming mice (8 weeks, female) were injected with 100 μL of WO_3 nanocapacitors (50 mg/kg) via the tail vein. Then, 10 μL blood was obtained from the tail vein at various time points of 5 min, 10 min, 0.5 h, 1 h, 2 h, 4 h, 8 h, 12 and 24 h postinjection. Next, the blood samples were diluted with 990 μL of deionized water containing 10 mM ethylenediaminetetraacetic acid disodium salt as a blood anticoagulant. The concentration of WO_3 (W element) was measured by ICP–OES. The biodistribution of WO_3 nanocapacitors in vivo was also determined using Kunming mice by intravenous injection of 100 μL of WO_3 nanocapacitors (50 mg/kg). After 24 h, the major organs (heart, liver, spleen, lung and kidney) were harvested and dissolved in aqua regia. Finally, the W element concentrations were detected by ICP–OES.

In vivo radiation therapy

To establish the xenograft tumour model, first, the xenograft tumour model was established by subcutaneously injecting Lewis cells (1×10^6 cells) into the flanks of Balb/c nude mice (7 weeks, female). When the tumour volume reached approximately 80–100 cm^3, the mice were randomly divided into four groups: (i) control, (ii) WO_3, (iii) Na_2WO_3, (IV) control + X-ray, (v) Na_2WO_3 + X-ray, and (vi) WO_3 + X-ray. PBS (10 μL), $Na_2WO_3{\cdot}2H_2O$ (1.4 mg, 10 μL) and WO_3 nanocapacitors (1 mg, 10 μL) were injected into tumours directly. After 12 h, the tumours of groups (iii, iv) were irradiated with 6 Gy X-rays. After 48 h, H&E and TUNEL staining of the tumour tissues was performed using commercially available kits. The body weight and tumour volume of the mice were measured every 3 days.

Results and discussion

Preparation and characterization of WO_3 nanocapacitors

WO_3 nanocapacitors containing oxygen vacancies (WO_{3-x}) were synthesized by the hydrothermal reaction between hydrochloric acid, $Na_2WO_4{\cdot}2H_2O$, sodium citrate, and glucose [30]. To eliminate vacancies, the as-prepared WO_{3-x} was calcined at 500 ℃ for 10 h. After heat treatment, pale yellow WO_3 nanocapacitors were obtained. Transmission electron microscopy (TEM) showed that the size of WO_3 was ~100 nm (Fig. 2a). The lattice distance ($d_{(200)}$ and $d_{(002)}$) in the high-resolution TEM (HRTEM) image (Fig. 2a) showed that the exposed crystal face was the (010) face. The hydrodynamic size of WO_3 measured by dynamic light scattering (DLS) was 145.1 nm (Fig. 2b), presenting the favourable water solubility of WO_3. The X-ray diffraction (XRD) peak confirmed the successful synthesis of WO_3 (Fig. 2c). The ultraviolet–visible (UV–Vis) spectrum revealed strong absorbance of WO_3 at approximately 400 nm (Figure S1).

Electrochemical measurements

After the successful preparation of WO_3 nanocapacitors, their electrochemical performance was investigated. The redox peaks in cyclic voltammograms (CV) fade away as the scanning speed increased, implying that WO_3 nanocapacitors were pseudocapacitors (Fig. 2d). The shape of the galvanostatic charge/discharge (GCD) curves and electrochemical impedance spectroscopy (EIS) further favoured that WO_3 was a pseudocapacitor (Fig. 2e and f), consistent with previous studies [31]. Using the GCD curves, the specific capacitance was calculated to be 236.5 F/g, 196.1 F/g, 191.8 F/g, 80.3 F/g at current densities of 0.5 A/g, 2.0 A/g, 5.0 A/g and 10.0 A/g, respectively. The cycling performance of WO_3 was also tested. As shown in Figure S2, after 5 thousand charge and discharge cycles at a current density of 5.0 A/g, the capacitance of WO_3 remained stable. All the electrochemical data concluded that WO_3 nanocapacitors had satisfying pseudocapacitance performance.

Regulating electron transportation in the process of radiolysis

As radiolysis could generate massive free electrons, these electrons would be partly absorbed by WO_3 nanocapacitors due to their pseudocapacitance effect. After irradiation with X-rays (100 Gy, 6 MeV), the photoluminescence (PL) spectrum of WO_3 nanocapacitors solutions (Fig. 3a and b) showed increased longwave fluorescence (625 nm ~ 675 nm) and decreased shortwave fluorescence (400 nm ~ 500 nm). This observation could be attributed to the changed energy band of WO_3 nanocapacitors

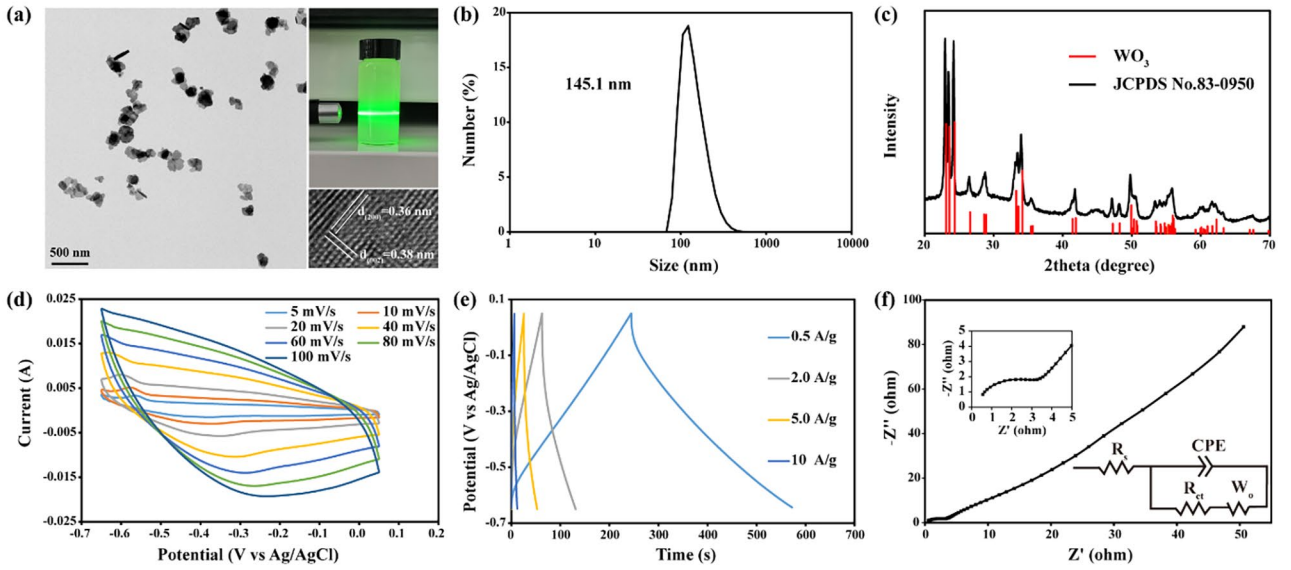

Fig. 2 Characterization of WO_3 nanocapacitors. **(a)** TEM, HRTEM and aqueous solutions images of WO_3 nanocapacitors. **(b)** Hydrodynamic size of WO_3 nanocapacitors. **(c)** X-ray diffraction pattern of WO_3. **(d)** Cyclic voltammograms of WO_3 nanocapacitors. **(e)** Galvanostatic charge/discharge curves of WO_3 nanocapacitors. **(f)** Electrochemical impedance spectroscopy of WO_3 nanocapacitors

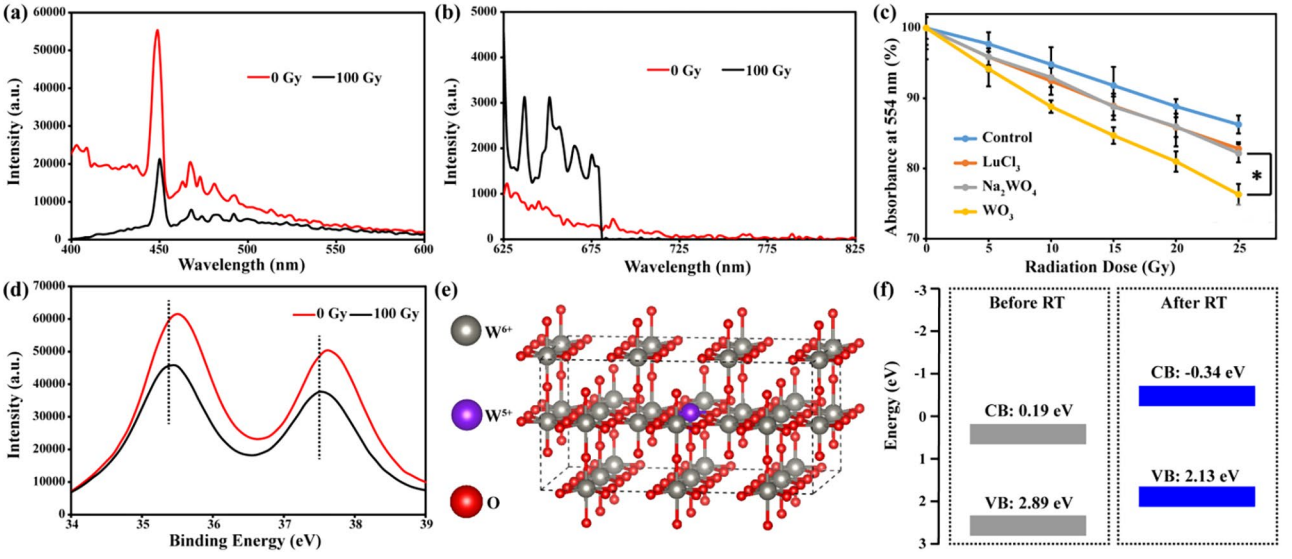

Fig. 3 Characterization of the interaction between WO_3 nanocapacitors and X-ray. **(a)** and **(b)** photoluminescence spectrum of WO_3 nanocapacitors before and after irradiation of 100 Gy X-rays, respectively. **(c)** The yield of ·OH in solutions upon irradiation of 0 Gy, 5 Gy, 10 Gy, 15 Gy, 20 and 25 Gy X-rays (n = 6, mean ± s.d., asterisk indicates $P < 0.05$ according to Student's two-tailed t test). **(d)** XPS spectra of WO_3 nanocapacitors before and after irradiation of 100 Gy X-rays. **(e)** Simulated WO_3 nanocapacitors lattice after accepting exogenous electrons. **(f)** Simulated conduction band and valence band before and after accepting exogenous electrons

induced by excess electrons, which further supported the experimental hypothesis [32, 33].

Radiotherapy utilizes reactive oxygen species, especially ·OH generation pathways for cancer treatment [6, 34]. The yield of ·OH in solutions was measured through the degradation of rhodamine B (RhB). As shown in Fig. 3c, the WO_3 group could induce more ·OH than the control groups, such as the $LuCl_3$ group and Na_2WO_4 group. The X-rays could decompose water into ·OH and electrons, while ·OH and electrons could neutralize each other by recombination. However, WO_3 could function as a pseudocapacitor to absorb electrons, resulting in reduced consumption of ·OH. While $LuCl_3$ and Na_2WO_4 existed in solution as ions, they cannot act as capacitors. These data also indicated that hexavalent W atoms made little contribution to the absorption of electrons because the yield of ·OH in the Na_2WO_4 (Z=74) group was similar to that in the $LuCl_3$ (Z=71) group.

We further investigated whether the electrons could be stored in WO_3 nanocapacitors. As shown in Fig. 3d, after X-ray irradiation, the binding energy of the W 4f orbital declined. Finally, a simulated calculation was conducted to assess the feasibility of regulating electron transportation. As shown in Fig. 3e, we set up a lattice containing W^{6+} and W^{5+} to simulate WO_3 nanocapacitors after RT. It was found that before RT, the conduction band of WO_3 was 0.19 eV; hence, free electrons in solutions (~-2.87 eV) could easily enter the lattice [35]. After receiving electrons, the conduction band of WO_3 was −0.34 eV, which could reduce NAD^+ to NADH (NAD^+/NADH~-0.32 eV). Both the experimental data and simulated calculation corroborated the feasibility of regulating electron transportation using WO_3 nanocapacitors.

In vitro cell experiments

After the experiments in solutions, in vitro experiments using Lewis cells (mouse lung cancer) were conducted. Firstly, we investigated the stability of WO_3 nanocapacitors in RPMI-1640 medium. Nonsignificant difference was detected in terms of hydrodynamic size (Figure S3) at 1-, 5- and 10-day period, respectively. In addition, few W atoms were released from WO_3 nanocapacitors as shown in Figure S4. These data showed that WO_3 nanocapacitors could remain stable in physiological solutions. Then, the cytotoxicity of WO_3 nanocapacitors was evaluated via CCK-8 assays. As shown in Figure S5, the viability of Lewis cells and normal cells (RAW264.7 and H9C2 cells) was more than 80%, even at a concentration of 400 μg/mL WO_3 nanocapacitors, and 20 μg/mL WO_3 nanocapacitors was used for the following cell experiments. $Na_2WO_3{\cdot}2H_2O$ (28.5 μg/mL) was also used as a control to balance the possible influence of W on radiation effects. Second, the intracellular content of •OH was detected. As shown in Fig. 4a, compared with the X-ray group and Na_2WO_3+X-ray group, the WO_3+X-ray group possessed a higher level of •OH, mainly attributed to the interference of the recombination between electrons and •OH.

In the process of RT, •OH attacks DNA molecules to cause SSBs and DSBs [36]. Although the amount of DNA SSBs is dozens of times that of DSBs, DNA DSBs are accountable for the majority of cancer cell deaths [19]. When DNA SSBs are not repaired in a timely manner, they will convert to fatal DSBs at replication forks [37]. The PARP-1-mediated signalling pathway is one of the most important DDR pathways responsible for DNA SSB repair. In the DNA damage repair process, the activation of PARP-1 occurs after its N-terminal zinc finger DNA binding domain recognizes and interacts with DNA SSBs. Subsequently, PARP-1 utilizes NAD^+ as a substrate to catalyse poly (ADP-ribose) (PAR) polymerization [37, 38]. The C-terminal domain then transfers PAR polymers to both itself and other neighbouring histones, which leads to the recruitment of various downstream proteins that participate in DNA repair [39]. Undoubtedly, NAD^+ is the essential substrate for PARP-1 enzymes. Therefore, reducing the intracellular NAD^+ content will restrain DNA SSB repair mediated by the PARP-1 signalling pathway and increase the number of irreparable DNA SSBs as well as the likelihood of DNA DSBs upon irradiation. As mentioned above, we found that WO_3 could increase the cellular content of •OH and was expected to decrease the content of NAD^+ upon irradiation. Hence, the NAD^+ consumption mediated by WO_3 nanocapacitors upon irradiation was expected to decrease the expression of PAR as well as the DNA SSB repair efficiency via the PARP-1 signalling pathway and induce more DSBs [40]. Subsequently, the intracellular NAD^+ content was detected to assess whether the released electrons can reduce intracellular NAD^+. After radiation, the ratio of NAD^+/NADH in cells obviously decreased in the presence of WO_3 nanocapacitors (Fig. 4b), indicating intracellular NAD^+ reduction, consistent with the results from the simulated calculation. Certainly, the decreased NAD^+ content would affect the expression of PAR protein.

To further visualize and quantify the impacts of WO_3 nanocapacitors on PAR, immunofluorescence staining of intracellular PAR was conducted. As shown in Fig. 4c, all the radiotherapy groups exhibited higher fluorescence intensity than the control group due to the activation of the PARP-1-mediated repair pathway. Meanwhile, the WO_3+X-ray group showed the mildest fluorescence intensity among the radiotherapy groups, indicating inhibited expression of PAR compared with the other two groups. Additionally, western blot analysis further proved the lower expression of PAR in the presence of WO_3 nanocapacitors upon irradiation (Fig. 4d). Both of these results demonstrated the decreased expression of PAR mediated by the reduced intracellular NAD^+ content, which further downregulated the activity of the PARP-1 signalling pathway. Consequently, more DNA DSBs were detected in the WO_3+X-ray groups (Fig. 5a). In line with these findings, the WO_3+X-ray group induced the highest apoptotic rate (Fig. 5d and c) and the lowest colony formation rate (Fig. 5d and Figure S6). Taken together, the in vitro experiments validated that WO_3 nanocapacitors could regulate electron transportation to improve the effect of RT by increasing the yield of •OH and inhibiting DNA damage repair.

In vivo animal experiments

The radiosensitizing effect of WO_3 nanocapacitors was further investigated using in vivo models. First, the in vivo biocompatibility of WO_3 nanocapacitors was tested using Kunming mice. The blood half-life of WO_3 nanocapacitors was approximately one hour (Figure S7), and it was mainly distributed in the liver and spleen after

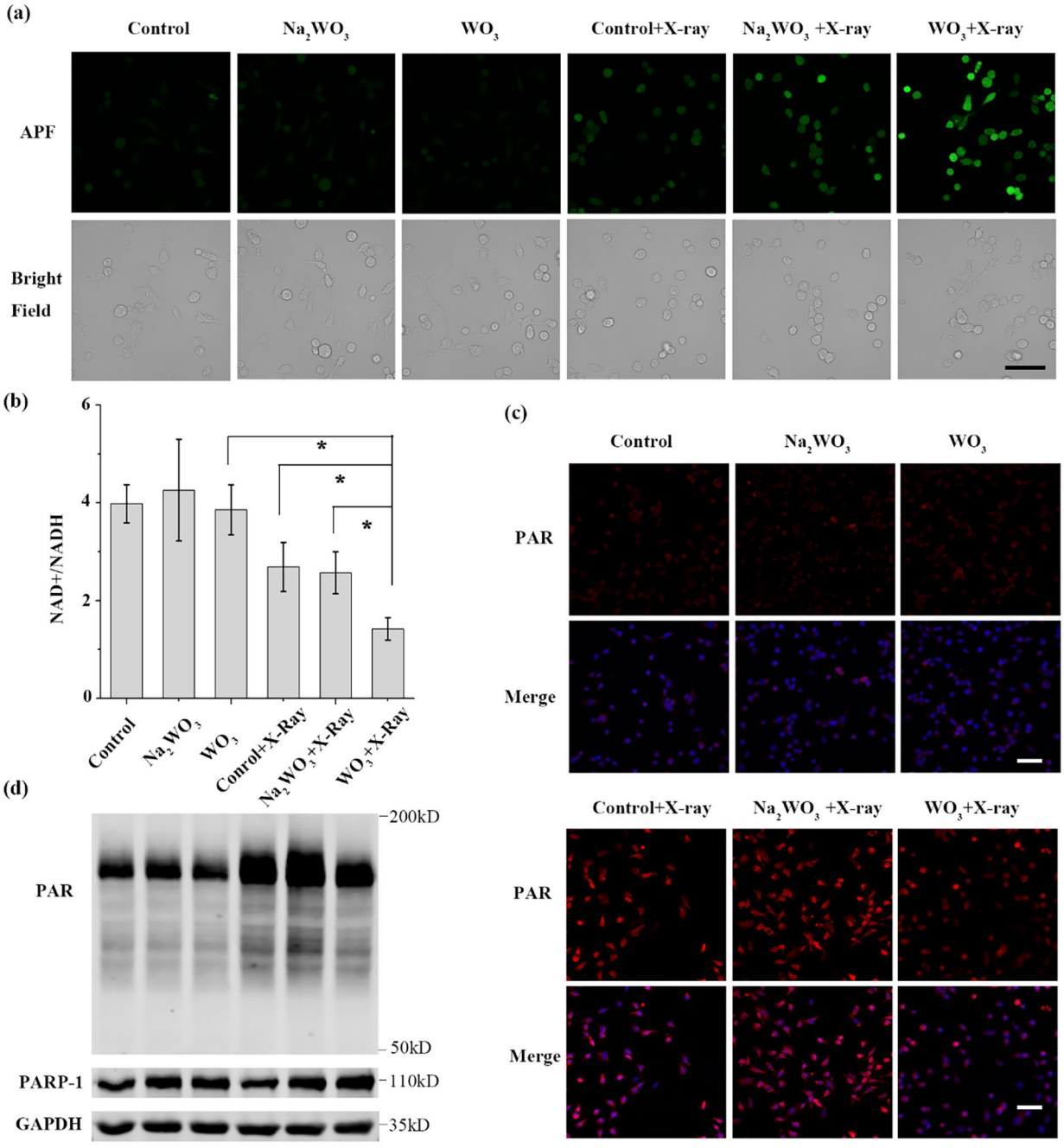

Fig. 4 In vitro cell experiments. **(a)** The yield of •OH (measured by APF probe). Scale bar: 50 μm. **(b)** The ration of NAD^+/NADH (n = 4, mean ± s.d., asterisk indicates $P < 0.05$ according to Student's two-tailed t test). **(c)** Immunofluorescence staining of intracellular PAR. Scale bar: 50 μm. **(d)** The content of PARP-1 and PAR.

intravenous injection (Figure S8). In line with the in vitro results, no obvious difference between the WO_3 group and the control group was observed in terms of body weight (Figure S9), haematological index (Figure S10), and histological examination of major organs (Figure S11), implying the favourable biocompatibility of WO_3 nanocapacitors. Then, tumour-bearing mouse models were established by subcutaneous inoculation of Lewis cells. After intratumoral administration of WO_3 solutions, the tumours were irradiated with 6 Gy of X-rays. The body weight and tumour size were recorded every third day for 15 days. The weight of the WO_3+X-ray group increased slightly, while the other groups showed varying degrees of weight loss (Fig. 6a). The WO_3+X-ray

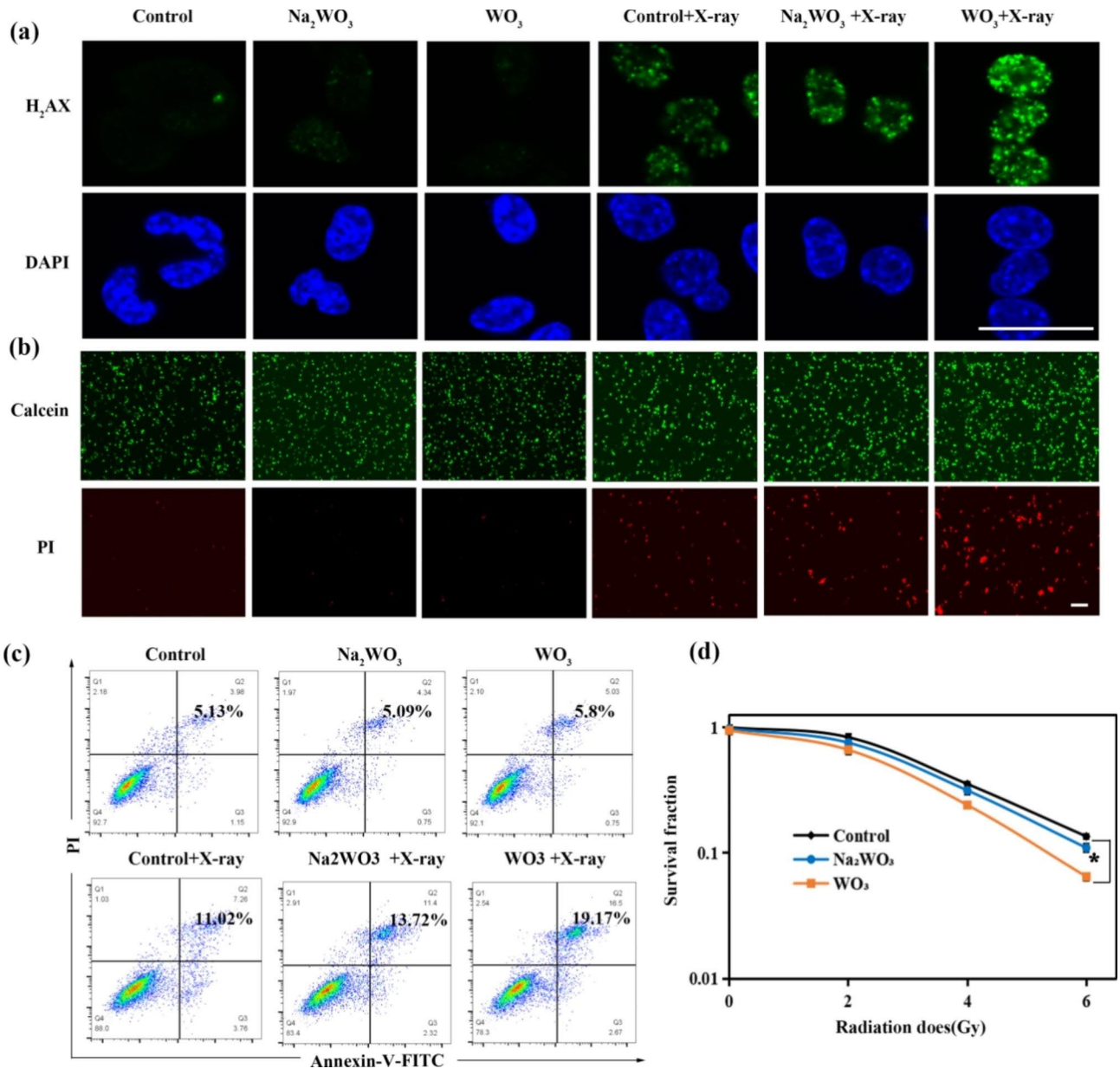

Fig. 5 In vitro cell experiments. **(a)** DNA DSBs (measured by γ-H_2AX staining). Scale bar: 50 μm. **(b)** The Staining of live(green) and dead(red) cells. Scale bar: 50 μm. **(c)** Apoptotic analysis measured by flow cytometry. **(d)** Cell survival assay using colony formation evaluation (n = 3, mean ± s.d., asterisk indicates $P < 0.05$ according to Student's two-tailed t test)

group showed the most significant tumour growth retardation compared with the other groups (Fig. 6b and S12). Based on H&E histological staining and terminal deoxynucleotidyl transferase-mediated nick end labelling (TUNEL) assays of tumours, the WO_3 + X-ray group presented the best therapeutic effect (Fig. 6c). Collectively, the in vivo experimental data validated the feasibility of WO_3 nanocapacitors-mediated electron-regulated radiosensitization.

Conclusion

In summary, this study provided a proof of concept of a novel radiosensitization approach based on WO_3 nanocapacitors by regulating electron transportation in situ. During radiolysis, WO_3 nanocapacitors absorbed electrons to prevent recombination between electrons and ·OH, contributing to a high cellular level of •OH. After radiolysis, the absorbed electrons were released to react with the PARP-1 substrate NAD^+. As a result, PARP-1-mediated DNA SSB repair was inhibited, which created more complicated DNA damage upon irradiation. The in vitro and in vivo experiments provided solid evidence for

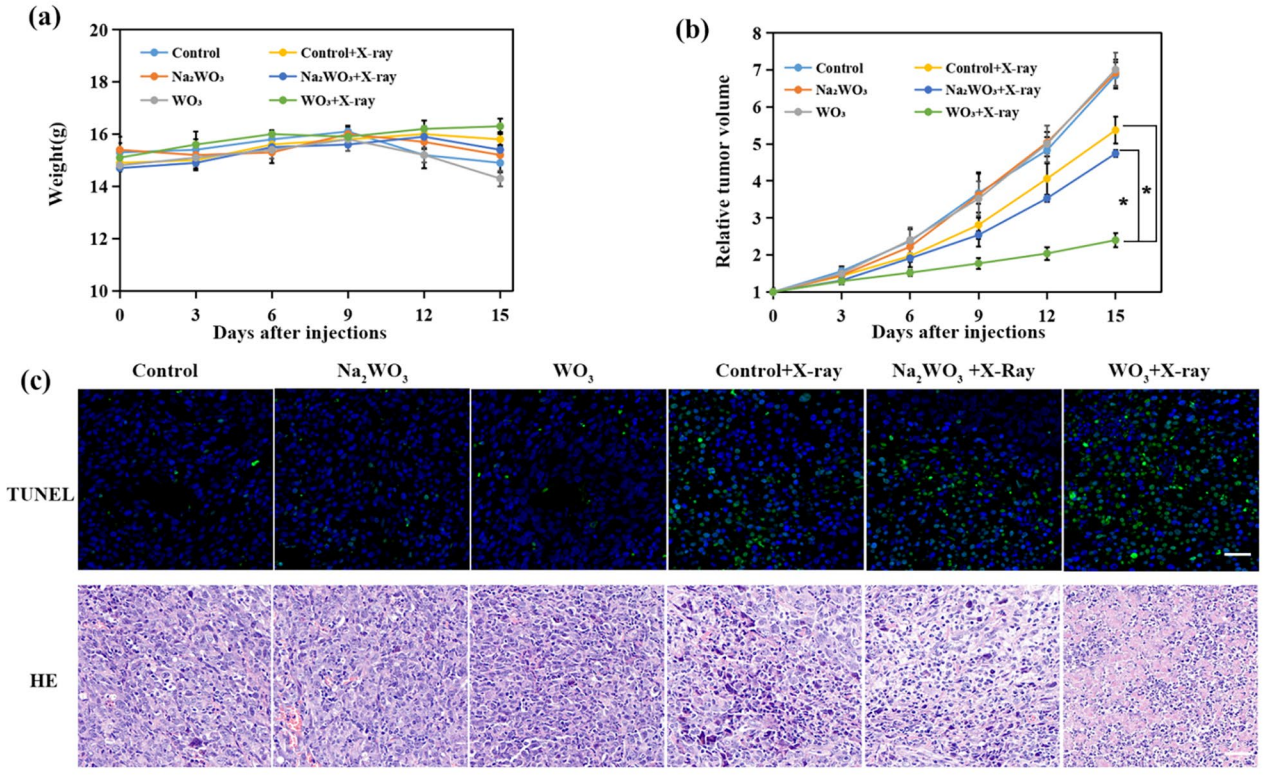

Fig. 6 In vivo experiments. **(a)** The change of weights of Lewis tumor-xenografted mice before and after irradiation of 6 Gy X-rays (n = 6, mean ± s.d.). **(b)** Relative tumor volume after intratumoral injection of PBS (10 μL), Na_2WO_3 and WO_3 nanocapacitors (1 mg, 10 μL) with or without irradiation of X-rays (6 Gy, n = 6, mean ± s.d., asterisk indicates $P < 0.05$ according to Student's two-tailed t test). **(c)** TUNEL staining and H&E staining of tumor sections. Scale bar: 50 μm

this hypothesis. Collectively, this strategy of nanocapacitor-based radiosensitization improves the radiotherapeutic effects by increasing the utilization of radiolytic electrons and ·OH, warranting further validation in multiple tumour models and preclinical experiments.

Supplementary Information

The online version contains supplementary material available at https://doi.org/10.1186/s12951-023-01962-8.

Supplementary Material 1

Authors' contributions

XPZ and YYL designed the research. HBG and LS carried out experiments and wrote the first draft of the paper. WBB,DLN,HW,LBZ, JJL,QWS and YW provided guidance and assistance on experiments. All authors reviewed the manuscript.

Funding

This work was partially supported by the National Funds for Distinguished Young Scientists (51725202), the Key Project of Shanghai Science and Technology Commission (19JC1412000), the National Natural Science Foundation of China (81472794), the National Science Foundation for the Young Scientists of China (51702211), the Shanghai Municipal Health Commission (2022JC006), the Shanghai Municipal Commission of Science and Technology (18441904400, 17411963600, 20S31903500), the Shanghai Sailing program (21YF1411500), the Shanghai Anticancer Association Eyas Project (SACA-CY19A04).

Data Availability

All study data are included in this article. Received: ((will be filled in by the editorial staff)). Revised: ((will be filled in by the editorial staff)). Published online: ((will be filled in by the editorial staff))

Declarations

Competing interests

The authors declare that they have no competing interests.

Supporting information

The online version contains supplementary materials available at (will be filled in by the editorial staff).

Ethics approval and consent to participate

All the experiments in vivo were approved by Animal Care Committee of laboratory animals of Fudan University.

Consent for publication

Not applicable.

Received: 6 May 2023 / Accepted: 17 June 2023
Published online: 29 June 2023

References

1. Herrera FG, Bourhis J, Coukos G. Radiotherapy combination opportunities leveraging immunity for the next oncology practice. CA Cancer J Clin. 2017;67:65–85.

2. Schaue D, McBride WH. Opportunities and challenges of radiotherapy for treating cancer. Nat Rev Clin Oncol. 2015;12:527–40.
3. Wang J, Li ZM, Wang ZT, Yu YH, Li D, Li BS, Ding JX. Nanomaterials for Combinational Radio-Immuno Oncotherapy. Adv Funct Mater 2020, 30.
4. Yong Y, Zhang CF, Gu ZJ, Du JF, Guo Z, Dong XH, Xie JN, Zhang GJ, Liu XF, Zhao YL. Polyoxometalate-based radiosensitization platform for treating hypoxic tumors by attenuating Radioresistance and Enhancing Radiation Response. ACS Nano. 2017;11:7164–76.
5. Song G, Cheng L, Chao Y, Yang K, Liu Z. Emerging nanotechnology and Advanced materials for Cancer Radiation Therapy. Adv Mater 2017, 29.
6. Wang H, Lv B, Tang Z, Zhang M, Ge W, Liu Y, He X, Zhao K, Zheng X, He M, Bu W. Scintillator-Based nanohybrids with Sacrificial Electron Prodrug for enhanced x-ray-induced photodynamic therapy. Nano Lett. 2018;18:5768–74.
7. Ni K, Lan G, Veroneau SS, Duan X, Song Y, Lin W. Nanoscale metal-organic frameworks for mitochondria-targeted radiotherapy-radiodynamic therapy. Nat Commun. 2018;9:4321.
8. Lan GX, Ni KY, Veroneau SS, Song Y, Lin WB. Nanoscale Metal-Organic Layers for Radiotherapy-Radiodynamic Therapy. J Am Chem Soc. 2018;140:16971–5.
9. James F, Wishart BR. *Recent Trends in Radiation Chemistry*; 2010.
10. Grand J, Ferreira SR, de Waele V, Mintova S, Nenoff TM. Nanoparticle alloy formation by Radiolysis. J Phys Chem C Nanomater Interfaces. 2018;122:12573–88.
11. Buxton G. *Radiation Chemistry: From Basics to Applications in Material and Life Sciences*; 2008.
12. Cubova K, Cuba V. Synthesis of inorganic nanoparticles by ionizing radiation - a review. Radiat Phys Chem Oxf Engl 1993. 2019;158:153–64.
13. Hengel SR, Spies MA, Spies M. Small-molecule inhibitors targeting DNA repair and DNA repair Deficiency in Research and Cancer Therapy. Cell Chem Biol. 2017;24:1101–19.
14. Jeggo PA, Pearl LH, Carr AM. DNA repair, genome stability and cancer: a historical perspective. Nat Rev Cancer. 2016;16:35–42.
15. Gavande NS, VanderVere-Carozza PS, Hinshaw HD, Jalal SI, Sears CR, Pawelczak KS, Turchi JJ. DNA repair targeted therapy: the past or future of cancer treatment? Pharmacol Ther. 2016;160:65–83.
16. Katsyuba E, Romani M, Hofer D, Auwerx J. NAD(+) homeostasis in health and disease. Nat Metab. 2020;2:9–31.
17. Yaku K, Okabe K, Hikosaka K, Nakagawa T. NAD metabolism in Cancer therapeutics. Front Oncol 2018, 8.
18. Sullivan-Reed K, Bolton-Gillespie E, Dasgupta Y, Langer S, Siciliano M, Nieborowska-Skorska M, et al. Simultaneous targeting of PARP1 and RAD52 triggers dual synthetic lethality in BRCA-Deficient tumor cells. Cell Rep. 2018;23:3127–36.
19. Hall EJ, Giaccia AJ. *Radiobiology for the radiologist: Seventh edition*; 2012.
20. Wishart J, Rao B. *Recent Trends in Radiation Chemistry*; 2010.
21. Yan JQ, Wang T, Wu GJ, Dai WL, Guan NJ, Li LD, Gong JL. Tungsten oxide single crystal nanosheets for enhanced Multichannel Solar Light Harvesting. Adv Mater. 2015;27:1580.
22. Zhang LL, Zhao XS. Carbon-based materials as supercapacitor electrodes. Chem Soc Rev. 2009;38:2520–31.
23. Wang Z, Gong WB, Wang XY, Chen ZG, Chen XL, Chen J, Sun HZ, Song G, Cong S, Geng FX, Zhao ZG. Remarkable Near-Infrared Electrochromism in Tungsten Oxide Driven by Interlayer Water-Induced battery-to-pseudocapacitor transition. ACS Appl Mater Interfaces. 2020;12:33917–25.
24. Wang YH, Wang CC, Cheng WY, Lu SY. Dispersing WO3 in carbon aerogel makes an outstanding supercapacitor electrode material. Carbon N Y. 2014;69:287–93.
25. Zheng F, Wang J, Liu WB, Zhou JM, Li H, Yu Y et al. Novel diverse-structured h-WO3 nanoflake arrays as electrode materials for high performance supercapacitors. Electrochim Acta 2020, 334.
26. Zhou Y, Li X, Lin H. To be higher and stronger-metal Oxide Electron Transport materials for Perovskite Solar cells. Small 2020, 16.
27. Wei WF, Cui XW, Chen WX, Ivey DG. Manganese oxide-based materials as electrochemical supercapacitor electrodes. Chem Soc Rev. 2011;40:1697–721.
28. Yu X, Yun S, Yeon JS, Bhattacharya P, Wang LB, Lee SW, Hu XL, Park HS. Emergent Pseudocapacitance of 2D nanomaterials. Adv Energy Mater 2018, 8.
29. Maiti S, Pramanik A, Mahanty S. Extraordinarily high pseudocapacitance of metal organic framework derived nanostructured cerium oxide. Chem Commun (Camb). 2014;50:11717–20.
30. Zhang N, Li XY, Liu YF, Long R, Li MQ, Chen SM, Qi ZM, Wang CM, Song L, Jiang J, Xiong YJ. Defective Tungsten Oxide Hydrate Nanosheets for Boosting Aerobic Coupling of Amines: Synergistic Catalysis by Oxygen Vacancies and Bronsted Acid Sites. *Small* 2017, 13.
31. Wu X, Yao SY. Flexible electrode materials based on WO3 nanotube bundles for high performance energy storage devices. Nano Energy. 2017;42:143–50.
32. Wang H, Gao H, Jiang X, Zhao P, Ni D, Tang Z, Liu Y, Zheng X, Bu W. Regulating water states by vacancies for cancer therapy. Nano Today. 2021;37:101099.
33. Su W, Wang H, Wang T, Li X, Tang Z, Zhao S, et al. Auger Electrons constructed active Sites on Nanocatalysts for Catalytic Internal Radiotherapy. Adv Sci (Weinh). 2020;7:1903585.
34. Jana D, Zhao Y. Strategies for enhancing cancer chemodynamic therapy performance. Exploration. 2022;2:20210238.
35. Matsui T, Kitagawa Y, Okumura M, Shigeta Y. Accurate Standard Hydrogen Electrode potential and applications to the Redox potentials of vitamin C and NAD/NADH. J Phys Chem A. 2015;119:369–76.
36. Xie J, Gong L, Zhu S, Yong Y, Gu Z, Zhao Y. Emerging strategies of nanomaterial-mediated Tumor Radiosensitization. Adv Mater. 2019;31:1802244.
37. Patel M, Nowsheen S, Maraboyina S, Xia F. The role of poly(ADP-ribose) polymerase inhibitors in the treatment of cancer and methods to overcome resistance: a review. Cell & Bioscience. 2020;10:35.
38. Du Z, Zhang X, Guo Z, Xie J, Dong X, Zhu S, Du J, Gu Z, Zhao Y. X-ray-controlled Generation of Peroxynitrite based on Nanosized LiLuF4:Ce3 + scintillators and their applications for Radiosensitization. Adv Mater. 2018;30:1804046.
39. Lin KY, Kraus WL. PARP inhibitors for Cancer Therapy. Cell. 2017;169:183.
40. Ivashkevich A, Redon CE, Nakamura AJ, Martin RF, Martin OA. Use of the γ-H2AX assay to monitor DNA damage and repair in translational cancer research. Cancer Lett. 2012;327:123–33.

Publisher's Note